

A statistical reconstruction algorithm for positronium lifetime imaging using time-of-flight positron emission tomography

Zheyuan Zhu, Hosna Tajvidi Safa, Chien-Min Kao, and Hsin-Hsiung Huang

Abstract—Positron emission tomography (PET) has been widely used for the diagnosis of serious diseases including cancer and Alzheimer’s disease, based on the uptake of radiolabelled molecules that target certain pathological signatures. Recently, a novel imaging mode known as positronium lifetime imaging (PLI) has been shown possible with time-of-flight (TOF) PET as well. PLI is also of practical interest because it can provide complementary disease information reflecting conditions of the tissue microenvironment via mechanisms that are independent of tracer uptake. However, for the present practical systems that have a finite TOF resolution, the PLI reconstruction problem has yet to be fully formulated for the development of accurate reconstruction algorithms. This paper addresses this challenge by developing a statistical model for the PLI data and deriving from it a maximum-likelihood algorithm for reconstructing lifetime images alongside the uptake images. By using realistic computer simulation data, we show that the proposed algorithm can produce quantitatively accurate lifetime images for a 570 ps TOF PET system.

Index Terms—Positron emission tomography, time-of-flight, positronium lifetime imaging, maximum likelihood.

I. INTRODUCTION

The physics that enables positronium lifetime imaging (PLI) with time-of-flight (TOF) positron emission tomography (PET) has recently been elucidated, and the feasibility of PLI has been experimentally demonstrated [1]–[3]. PET is widely used for revealing the functional state of an organ or tissue by the uptake of a specific PET molecule as governed by its physiological and biochemical interactions with the body. On the other hand, PLI measures the lifetime of positronium, which is a meta-stable electron-positron pair formed by a positron released by a PET molecule [4]. Interactions between positronium and nearby molecules such as oxygen that contain an unpaired electron will shorten its lifetime. Therefore, the positronium lifetime can quantitatively reflect the presence and concentration of such molecules in the tissue microenvironment independent of the uptake mechanism of the PET molecule. This is of clinical interest because, for example, hypoxic tissues are resistant to many therapeutics [5], [6]. Knowing the local tissue oxygenation may lead to better treatment outcomes for cancer. Also, PLI could open the door for the creation of novel contrast mechanisms for PET.

Presently, PLI is demonstrated under the assumption of perfect TOF resolution so that events can be precisely localized

This work was partially supported by NSF grant DMS-1924792 and NIH grant R01-EB029948.

Z. Zhu is with CREOL, The College of Optics and Photonics, University of Central Florida, Orlando, FL 32816 (e-mail: zyzhu@knights.ucf.edu)

C.-M. Kao is with Department of Radiology, University of Chicago, Chicago, IL 60637 (e-mail: ckao95@uchicago.edu).

H.-H. Huang (the corresponding author) is with Department of Statistics and Data Science, University of Central Florida, Orlando, FL 32816 (email: hsin.huang@ucf.edu)

to their origins in space [7], [8]. However, the present TOF PET systems have a resolution in the range of 200 - 600 ps FWHM [9]–[11], corresponding to a spatial resolution of 3-9 cm. For such systems, the naive reconstruction method using backprojection yields PLI images that have poor resolution and are likely to be quantitatively inaccurate. Therefore, PLI reconstruction under finite TOF resolutions is a topic of interest and significance.

This issue potentially can be addressed by the development of a statistical model relating the unknown uptake and lifetime images to the PLI data to allow inversion of the data. So far, this idea has only been investigated by Qi and Huang [12]. In their model, the lifetime measurement does not include the effects of the finite time resolution of the detectors or the difference in the flight time of the gamma rays associated with an event before they are detected. We proposed a novel image reconstruction method using the estimated time delay $\hat{\tau}_k$, while Qi and Huang (2022) [12] employ the theoretical (the true) time delay τ_k . The main contribution of this paper is the development of a more complete model for the PLI data. We also develop a compute-efficient gradient-based iterative reconstruction algorithm for producing the maximum likelihood (ML) estimator of this model. Using computer-simulated data, we demonstrate that the resulting algorithm can accurately recover the lifetime image from data acquired by a 570 ps TOF PET system.

The remainder of this paper is organized as follows. Section II formulates the statistical model for the PLI list-mode data and uses the model to develop an algorithm for obtaining the maximum likelihood estimates of both uptake and lifetime images. Section III describes the computer-simulation study and presents the results. Section IV provides a summary and conclusion.

II. STATISTICAL MODEL FOR PLI

A. Detection of a PLI event

Figure 1 illustrates the use of a two-dimensional (2d) TOF PET system that consists of a ring of uniformly spaced detectors for PLI. The detectors are labeled numerically by an index variable i . Contrary to the traditional PET, PLI uses an isotope such as Sc-44 that emits a positron and a prompt gamma essentially at the same time [13], [14]. Suppose that an isotope decay occurs at location \mathbf{r}_{decay} at time t_{decay} . As depicted by the blue line in the figure, the prompt gamma travels a distance α_γ from \mathbf{r}_{decay} towards the detector ring at a random angle ϕ_γ , detected by detector i_γ at time $t_\gamma = t_{decay} + \alpha_\gamma/v_c$, where v_c is the speed of light.

On the other hand, the released positron annihilates after

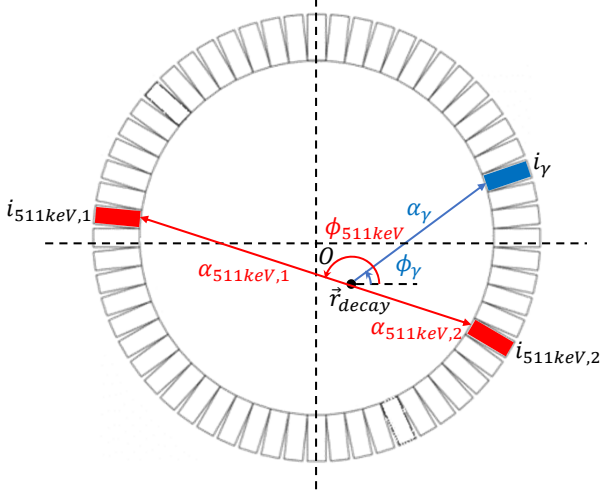


Fig. 1. Detection of a PLI event using 2-d TOF PET system.

some time τ that follows an exponential distribution

$$p_{pd}(\tau; \lambda) = \lambda e^{-\lambda \tau}. \quad (1)$$

The exponential distribution in Equation (1) is reasonable for the tail part of the positron annihilation lifetime distribution. Please see Figure 5 in [7]. The decay rate constant λ (whose inverse λ^{-1} is the lifetime) depends on the condition surrounding the positronium. The red line in the Fig. 1 illustrates the two opposite 511 keV gamma rays by annihilation. They travel from \mathbf{r}_{decay} at a random angle ϕ_{511keV} and are detected by detectors $i_{511keV,1}$ and $i_{511keV,2}$ at time $t_{511keV,1} = t_{decay} + \tau + \alpha_{511keV,1}/v_c$ and $t_{511keV,2} = t_{decay} + \tau + \alpha_{511keV,2}/v_c$ respectively, where $\alpha_{511keV,1}$ and $\alpha_{511keV,2}$ are the distances these photons travel.

The conventional TOF PET system reports $i_{511keV,1}$, $i_{511keV,2}$, and the TOF given by

$$\Delta t_{511keV} = t_{511keV,1} - t_{511keV,2} = (\alpha_{511keV,1} - \alpha_{511keV,2})/v_c. \quad (2)$$

We assume that the system is extended to be capable of triple-coincidence detection and reports additionally i_γ and

$$\begin{aligned} \Delta t_\gamma &= (t_{511keV,1} + t_{511keV,2})/2 - t_\gamma \\ &= \tau + (\alpha_{511keV,1} + \alpha_{511keV,2} - 2\alpha_\gamma)/(2v_c). \end{aligned} \quad (3)$$

Note that $\alpha_{511keV,1} + \alpha_{511keV,2}$ can be determined from $i_{511keV,1}$ and $i_{511keV,2}$ because it equals the distance between the corresponding detectors. Also, if Δt_{511keV} is exactly known, \mathbf{r}_{decay} can be identified, and then α_γ can be computed from i_γ and \mathbf{r}_{decay} . Then, Eq. (3) can be used to compute τ from Δt_γ .

In a practical system, the time measurement has limited precision and is typically binned and stored as integers. Below, we shall use c to denote a triplet consisting of $i_{511keV,1}$, $i_{511keV,2}$, and binned Δt_{511keV} measured for an event. TOF resolution refers to the uncertainty of Δt_{511keV} in FWHM. With a finite TOF resolution, \mathbf{r}_{decay} cannot be precisely determined. For a 200 ps (600 ps) system, this leads to a 3 cm (9 cm) uncertainty in \mathbf{r}_{decay} . Similarly, Δt_γ has limited precision and is binned. Hence, in Eq. (3) α_γ is not precisely known and all the time measurements involved contain statistical variations.

We assume that the uncertainty in time measurement by all detectors is identical and independent, modelled by a one-dimensional (1-d) Gaussian distribution $N(0, \sigma)$. Then, from Eqs. (2) and (3) we have $\sigma\{\Delta t_{511keV}\} = \sqrt{2}\sigma$ and $\sigma\{\Delta t_\gamma\} = \sqrt{3/2}\sigma$. Under this assumption, the resolution in Δt_γ therefore equals the TOF resolution of the system multiplied by $\sqrt{3}/2$.

B. Probability model of the PLI list-mode data

Generally, the detected PLI events are stored as a list of $w_k = (c_k, i_{\gamma,k}, \Delta t_{\gamma,k})$, $k = 1, \dots, N_k$, where $i_{\gamma,k}$, c_k are the TOF channel and detector that receives the prompt gamma and annihilation gamma pair within the triple coincident event k , $\Delta t_{\gamma,k}$ is the time difference between the detections of prompt and annihilation gamma rays, and N_k is the total number of events acquired, yielding the list-mode (LM) data $\mathcal{W}_{N_k} = \{w_k\}_{k=1}^{N_k}$. The PLI LM data includes the traditional TOF PET LM data $\mathcal{C}_{N_k} = \{c_k\}_{k=1}^{N_k}$.

We consider voxelized images $\mathbf{f} = [f_j]$ and $\boldsymbol{\lambda} = [\lambda_j]$, where $f_j \geq 0$ and $\lambda_j \geq 0$ are the PET isotope concentration and positronium decay rate constant within voxel (which is also a pixel in 2d image slices) j . We derive maximum likelihood estimation (MLE) based on the true τ_k like the model in [12], and denote the PLI LM data as $\mathcal{W}_{N_k}^0 = \{w_k^0\}_{k=1}^{N_k}$, where $w_k^0 = (c_k, \tau_k)$. However, we use the estimated τ_k introduced in Equation (15) for our image reconstruction experiments since the true τ_k is not directly observed with a finite CRT.

The MLE based on the log-likelihood of $(\boldsymbol{\lambda}, \mathbf{f})$ given $\mathcal{W}_{N_k}^0$ is

$$\arg \max_{\boldsymbol{\lambda}, \mathbf{f}} \ell(\boldsymbol{\lambda}, \mathbf{f}; \mathcal{W}_{N_k}^0) = \arg \max_{\boldsymbol{\lambda}, \mathbf{f}} \sum_{k=1}^{N_k} \log \left(\sum_{j=1}^{N_j} H_{c_k, j} f_j \lambda_j e^{-\lambda_j \tau_k} \right), \quad (4)$$

and the MLE of \mathbf{f} based on the marginal log-likelihood of \mathbf{f} given \mathcal{C}_{N_k} is

$$\arg \max_{\mathbf{f}} \ell(\mathbf{f}; \mathcal{C}_{N_k}) = \arg \max_{\mathbf{f}} \sum_{k=1}^{N_k} \log \left(\sum_{j=1}^{N_j} H_{c_k, j} f_j \right), \quad (5)$$

where N_j be the number of image voxels and $H_{c_k, j}$ is the probability for a PLI event originating from voxel j to be detected by channel c_k . Please read the details about the log-likelihoods in the Appendix.

C. Maximum likelihood estimation

The ML estimates for \mathbf{f} and $\boldsymbol{\lambda}$ are obtained from the above log likelihoods using gradient-based methods. The gradient of $\ell(\boldsymbol{\lambda}, \mathbf{f}; \mathcal{W}_{N_k}^0)$ with respect to $\boldsymbol{\lambda}$ is given by

$$\frac{\partial \ell(\boldsymbol{\lambda}, \mathbf{f}; \mathcal{W}_{N_k}^0)}{\partial \lambda_j} = \sum_{k=1}^{N_k} \frac{H_{c_k, j} f_j (1 - \tau_k \lambda_j) e^{-\lambda_j \tau_k}}{\sum_{j=1}^{N_j} H_{c_k, j} f_j \lambda_j e^{-\lambda_j \tau_k}}. \quad (6)$$

The gradient of $\ell(\mathbf{f}; \mathcal{C}_{N_k})$ with respect to \mathbf{f} is

$$\frac{\partial \ell(\mathbf{f}; \mathcal{C}_{N_k})}{\partial f_j} = \sum_{k=1}^{N_k} \frac{H_{c_k, j}}{\sum_{j=1}^{N_j} H_{c_k, j} f_j + \varepsilon}, \quad (7)$$

where ε is a small positive number (i.e., 1.0×10^{-10}) introduced to improve numerical stability when $\sum_j H_{c_k, j} f_j$ is

small. The reconstruction algorithm starts with uniform initial estimates of \mathbf{f} and $\boldsymbol{\lambda}$, specifically, $\hat{\mathbf{f}}^{(0)} = N_k/N_j$ and $\hat{\boldsymbol{\lambda}}^{(0)} = \mathbf{0}$. We first obtain the ML estimate for \mathbf{f} by using the following iterations:

$$\hat{\mathbf{f}}^{(n)} = \hat{\mathbf{f}}^{(n-1)} + \eta_{\mathbf{f}} \times \left. \frac{\partial \ell(\mathbf{f}; \mathcal{C}_N)}{\partial \mathbf{f}} \right|_{\mathbf{f}=\hat{\mathbf{f}}^{(n-1)}}. \quad (8)$$

After $\hat{\mathbf{f}}_{\text{ML}}$ is obtained, the ML estimate for $\boldsymbol{\lambda}$ is obtained by

$$\hat{\boldsymbol{\lambda}}^{(n)} = \hat{\boldsymbol{\lambda}}^{(n-1)} + \eta_{\boldsymbol{\lambda}} \times \left. \frac{\partial \ell(\boldsymbol{\lambda}, \mathbf{f}; \mathcal{W}_N^0)}{\partial \boldsymbol{\lambda}} \right|_{\mathbf{f}=\hat{\mathbf{f}}_{\text{ML}}, \boldsymbol{\lambda}=\hat{\boldsymbol{\lambda}}^{(n-1)}}. \quad (9)$$

In Eqs. (8) and (9), the step sizes $\eta_{\mathbf{f}}$ and $\eta_{\boldsymbol{\lambda}}$ were empirically chosen to be 0.1 and 0.00002, respectively. Unless mentioned otherwise, 30000 and 500 iterations were used for Eqs. (8) and (9) respectively. The nonnegativity conditions $\mathbf{f}, \boldsymbol{\lambda} \geq 0$ are imposed by setting any negative f_j and λ_j to zero during iterations.

III. COMPUTER-SIMULATION STUDIES

A. Data generation

The PLI LM data \mathcal{W}_{N_k} was generated by Monte-Carlo methods for a scanner that consists of N_{det} detectors uniformly spaced on a ring of diameter D . Given \mathbf{f} , an image pixel j is randomly sampled according to \mathbf{f} (given a decay, f_j gives the relative probability for it to occur in pixel j). Then, a point $\mathbf{r}_{decay} = (x_{decay}, y_{decay})^T$ that falls inside the area of the pixel $A_j = [x_j, x_j + \Delta x] \times [y_j, y_j + \Delta y]$, where Δx and Δy are the pixel sizes along the x and y directions, is sampled from \mathcal{U}_{A_j} , where \mathcal{U}_S represents a uniform distribution over set S . A prompt gamma is emitted at \mathbf{r}_{decay} at an angle ϕ_γ that is sampled from $\mathcal{U}_{[0, 2\pi]}$. Then, α_γ , the distance the prompt gamma travels before detection, is a solution of the following equation

$$|\mathbf{r}_{decay} + \alpha_\gamma \hat{\boldsymbol{\phi}}_\gamma| = D/2, \quad (10)$$

where $\hat{\boldsymbol{\phi}} = (\cos \phi, \sin \phi)^T$ is the unit vector in the direction of ϕ . This equation has two solutions given by

$$\alpha_\gamma^\pm = -\hat{\boldsymbol{\phi}}_\gamma^T \mathbf{r}_{decay} \pm \sqrt{(\hat{\boldsymbol{\phi}}_\gamma^T \mathbf{r}_{decay})^2 - \|\mathbf{r}_{decay}\|^2 + D^2/4}. \quad (11)$$

These solutions correspond to the distances traveled in angle ϕ_γ and $-\phi_\gamma$. Since ϕ_γ is sampled from $\mathcal{U}_{[0, 2\pi]}$, we can arbitrarily choose one of these solutions, say α_γ^+ , without affecting the distribution of α_γ . The detector i_γ is determined using the location $\mathbf{r}_{detect} = \mathbf{r}_{decay} + \alpha_\gamma^+ \hat{\boldsymbol{\phi}}_\gamma$, which is where the prompt gamma hits the detector ring, by

$$i_\gamma = \left\lceil \left(\frac{N_{det}}{2\pi} \right) \angle \mathbf{r}_{detect} \right\rceil, \quad (12)$$

where $\angle \mathbf{r}$ denotes the angle of \mathbf{r} and $\lceil x \rceil$ is the largest integer that is smaller than or equal to x .

For the annihilation photons, we also sample an emission angle ϕ_{511keV} from $\mathcal{U}_{[0, 2\pi]}$. Replacing ϕ_γ in Eq. (11) with ϕ_{511keV} yields two solutions α_{511keV}^\pm , which are the distances traveled by the two opposite photons. We then employ Eq. (12) with obvious substitutions to obtain $i_{511keV,1}$ and $i_{511keV,2}$. Also,

$$\Delta t_{511keV}^0 = (\alpha_{511keV}^+ - \alpha_{511keV}^-)/v_c. \quad (13)$$

To obtain Δt_γ , the time between isotope decay and annihilation τ is sampled from the exponential distribution $p_{pd}(\tau; \lambda_j)$. Then, we use Eq. (3) to compute

$$\Delta t_\gamma^0 = \tau + (\alpha_{511keV,1}^+ + \alpha_{511keV,1}^- - 2\alpha_\gamma)/(2v_c). \quad (14)$$

The above procedures do not include uncertainties in time measurement and binning. As discussed in Sect. II-A, given a coincidence resolving time (CRT) of interest, a number δt_1 is drawn from a zero-mean Gaussian distribution $N(0, \sigma_t)$, where $\sigma_t = CRT/(2\sqrt{2\ln 2})$, and then the TOF of the event is given by $\Delta t_{511keV} = \Delta t_{511keV}^0 + \delta t_1$. Likewise, $\Delta t_\gamma = \Delta t_\gamma^0 + \delta t_2$ where δt_2 is drawn from $N(0, \sqrt{3}\sigma_t/2)$. Then, Δt_{511keV} and Δt_γ are discretized according to the width of the time bin of the simulated system.

B. Calculation of the system matrix

The system matrix $\mathbf{H} = [H_{c_k, j}]$ used in Eqs. (8) and (9) for image reconstruction is precomputed and stored as follows. We have previously implemented a multi-ray tracing method [15] for computed tomography. This method identifies the image pixels that a line intersects with as well as the intersection points with the boundaries of these pixels. Given a line-of-response (LOR) of the TOF PET system, we apply this method to locate all intersecting pixels and locations. We then calculate the contributions of each intersecting pixel to all the time bins on this LOR by $w = \exp\{-d^2/2\sigma_r^2\}$, where $\sigma_r = v_c \sigma_t$ and d is the distance between the location given by the center of the time bin and the center of the intersecting LOR segment with the pixel. This w is assigned to $H_{c_k, j}$ according to the LOR, time bin, and intersecting pixels. Subsequently, \mathbf{H} is normalized so that $\sum_k H_{c_k, j} = 1$, i.e., the positron emission events from pixel j are detected by channel c_k with probability $H_{c_k, j}$.

C. Simulation setup

We generated PLI LM data as described in Sec. III with $N_{det} = 288$, $D = 57$ cm, and $CRT = 570$ ps. Fourteen 400-ps-width time bins were used. These settings yield 1.16 million TOF PET channels (i.e. the number of allowed values for c).

The proposed reconstruction algorithm for $\boldsymbol{\lambda}$ is based on τ , which, as discussed above, is not available with a finite CRT. Nonetheless, in this work we applied Eq. (3) to obtain an estimate $\hat{\tau}$ from w by

$$\hat{\tau} = \Delta t_\gamma - (L_{i_{511keV,1}, i_{511keV,2}} - 2\hat{\alpha}_\gamma)/(2v_c), \quad (15)$$

where $L_{i_{511keV,1}, i_{511keV,2}} = \alpha_{511keV,1}^+ + \alpha_{511keV,1}^-$ is the distance between detectors $i_{511keV,1}$ and $i_{511keV,2}$, and $\hat{\alpha}_\gamma$ is the distance between detector i_γ and the decay location identified by $i_{511keV,1}$, $i_{511keV,2}$, and Δt_{511keV} . The estimate $\hat{\tau}$ was used in place of τ for image reconstruction.

As in [12], λ_j^{-1} was also estimated by backprojecting the events into pixels according to \mathbf{H} and then taking the average of $\hat{\tau}_k$. For each pixel j ,

$$(\hat{\boldsymbol{\lambda}}_{BP})_j^{-1} = \sum_k H_{c_k, j} \hat{\tau}_k. \quad (16)$$

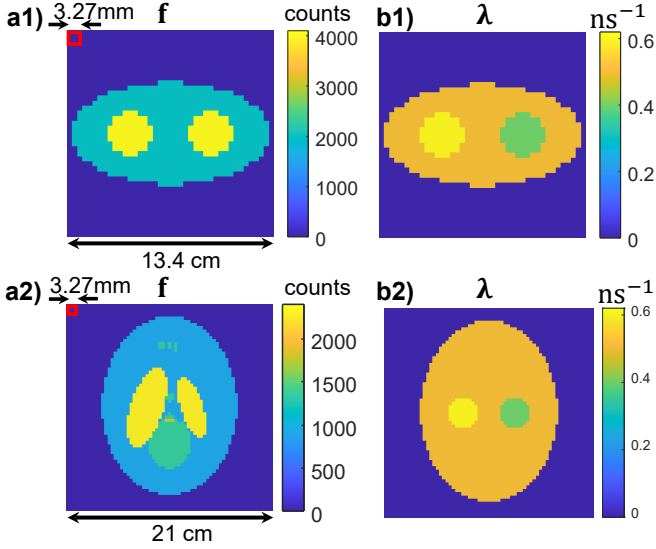


Fig. 2. Activity images (left column) and rate-constant images (right column) of phantom 1 (top row) and phantom 2 (bottom row). These images consists of 3.27×3.27 mm² square pixels.

Below, we shall refer to the above and proposed reconstruction methods as BP and ML, respectively.

We considered two numerical phantoms, shown in Fig. 2, for evaluating the proposed reconstruction method. Phantom 1 has a uniform elliptical activity map measuring 13.0 cm and 6.5 cm along the major and minor axes, respectively. Its rate-constant image contains two discs that have different λ values (0.4 and 0.6 ns⁻¹) from the background ellipse (0.5 ns⁻¹). Phantom 2 is a modified Shepp-Logan phantom measuring 18 cm by 13.7 cm along its major and minor axis respectively. The rate-constant image contains two 3.2 cm diameter discs with different λ values (0.4 and 0.6 ns⁻¹) from the background (0.5 ns⁻¹). The expected number of events to generate were 1.4 million and 2.2 million, respectively, for phantom 1 and phantom 2. Here we only consider valid triple-coincidence events described by $w_k = (c_k, \tau_k)$. The effects of attenuation, scattering, and random events are beyond the scope of this manuscript, and hence not included in the simulation. All images are discretized into square pixels of 3.27×3.27 mm², with 41×41 pixels for phantom 1, and 65×65 pixels for phantom 2.

IV. RESULTS

A. Activity and decay rate constant reconstruction

Figure 3 compares images obtained for phantom 1 by the ML and BP methods. We also quantify the reconstruction accuracy with the normalized mean square error (NMSE), defined by

$$\text{NMSE} = \frac{\|\hat{\lambda} - \lambda\|^2}{\|\lambda\|^2}, \quad (17)$$

where $\hat{\lambda}$ and λ are the reconstructed and ground-truth images, respectively, and $\|\cdot\|$ is the L-2 norm. A 570 ps CRT corresponds to a spatial uncertainty of 8.5 cm, which is larger than half of the largest dimension of the phantom. As a result,

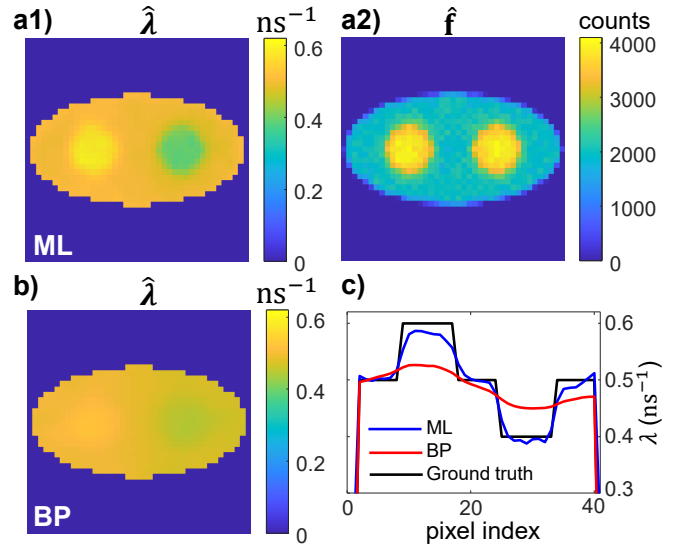


Fig. 3. Results obtained for phantom 1. (a1 & a2) $\hat{\lambda}_{ML}$ and \hat{f}_{ML} produced by the proposed reconstruction method. (b) $\hat{\lambda}_{BP}$ produced by using Eq. (16). (c) Horizontal profiles across the center of the reconstructed images $\hat{\lambda}_{ML}$ and $\hat{\lambda}_{BP}$, and of the ground-truth image λ .

Fig. 3(b) shows a significantly blurred $\hat{\lambda}_{BP}$ and the two discs can be barely seen. In contrast, Fig. 3(a1) shows that the two discs are distinct from the background in $\hat{\lambda}_{ML}$ obtained by the proposed method. Their edges are also well identifiable. Figure 3(c) compares the horizontal profiles across the center of the reconstructed and ground-truth images, showing that the profile of $\hat{\lambda}_{ML}$ agrees with the truth and that of $\hat{\lambda}_{BP}$ is almost flat. The NMSEs of $\hat{\lambda}_{ML}$ and $\hat{\lambda}_{BP}$ are 3.1×10^{-5} and 2.4×10^{-4} , respectively, indicating that ML method is substantially more accurate than the BP method.

Figure 4 similarly shows the results obtained for phantom 2. The NMSEs of $\hat{\lambda}_{ML}$ and $\hat{\lambda}_{BP}$ are 3.5×10^{-5} and 2.7×10^{-4} , respectively. The two disc regions, 0.4 ns⁻¹ and 0.6 ns⁻¹, can be clearly distinguished from the background, 0.5 ns⁻¹, thanks to the achieved spatial resolution beyond CRT limit in ML estimations. It is worth noting that CRT contributes to the resolvable decay rate constant features in two aspects. First, CRT introduces spatial blurring that renders neighbouring features in λ indistinguishable. Second, CRT introduces errors in the estimated time delay $\hat{\tau}_k$ from each event. In our cases, the 570 ps (0.57 ns) CRT is comparable to the differences in lifetime among the background (2 ns) and the two disc regions (2.5 ns and 1.67 ns, respectively). If the difference in the lifetime between two regions is much smaller than CRT, for example, a 0.45 ns⁻¹ region against 0.5 ns⁻¹ background with only 0.2 ns difference in lifetime, the contrast between these regions may not be clearly resolved in the ML-estimated λ map.

Observe that f and λ of this phantom have different spatial patterns. Since estimation of λ is dependent on f , potentially the resulting λ can contain patterns of f if the reconstruction method is not accurate. Here we quantify the crosstalk between the activity map and the decay rate constant map with the cross-correlation, normalized by the L2-norms of f and λ , as

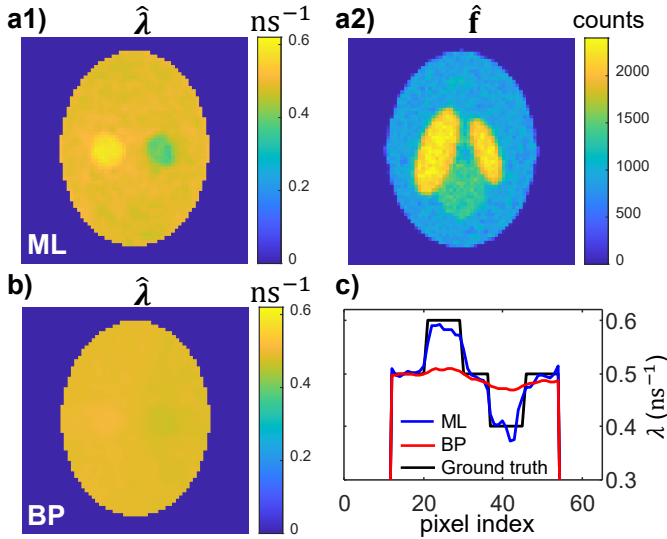


Fig. 4. Results obtained for phantom 2. (a1&a2) $\hat{\lambda}_{ML}$ and \hat{f}_{ML} produced by the proposed reconstruction method. (b) $\hat{\lambda}_{BP}$ produced by using Eq. (16). (c) Horizontal profiles across the center of the reconstructed images $\hat{\lambda}_{ML}$ and $\hat{\lambda}_{BP}$, and of the ground-truth image λ .

in Eq 18.

$$C := \frac{(\hat{\lambda} - \lambda)^T \cdot \mathbf{f}}{\|\lambda\| \|\mathbf{f}\|}. \quad (18)$$

The 0.18% and 1.3% cross-correlations in the ML-estimations of phantoms 1 and 2 quantitatively indicate that the crosstalk from \mathbf{f} into the ML-estimated λ is negligible. The results again show that the BP method cannot produce a useful estimate of λ given the poor CRT of the simulated system, but the proposed method can produce a qualitatively and quantitatively better estimate of λ .

B. Effects of CRT in ML-reconstruction

The choice of 570 ps CRT in Sec. IV.A reflects the performance of EXPLORER whole-body scanner. To understand the effect of different CRTs on our ML-based reconstruction method, we performed reconstructions from simulated events with CRTs ranging from 200 ps to 1600 ps using a phantom with activity and decay rate constant maps shown in Figure 5. We selected the width of time bin according to the CRT $\delta t \leq CRT/\sqrt{2\ln 2}$, and we ensured the total number of time bins, N_{bins} can fully cover the phantom $N_{bins} > (D/v_c + CRT)/\delta t$, where D is the phantom diameter. We maintained the same number of total events, 1 million, in generating all the list mode events. With each given CRT, 5 independent Monte Carlo instances were generated for testing the reconstruction performance. Figure 5(c) plots the average and standard deviation of the NMSE of the reconstructed decay rate constant map. A reconstruction instance of each CRT is plotted in Figure 5(d). The results show that a smaller CRT does not always contribute to better reconstruction. From a probabilistic view, a finite CRT essentially performs a projection of pixels along the LOR. Small CRT, such as 200 ps, covers a segment of only 3 cm along the LOR, which is smaller than the phantom size and could result in interior artifacts commonly

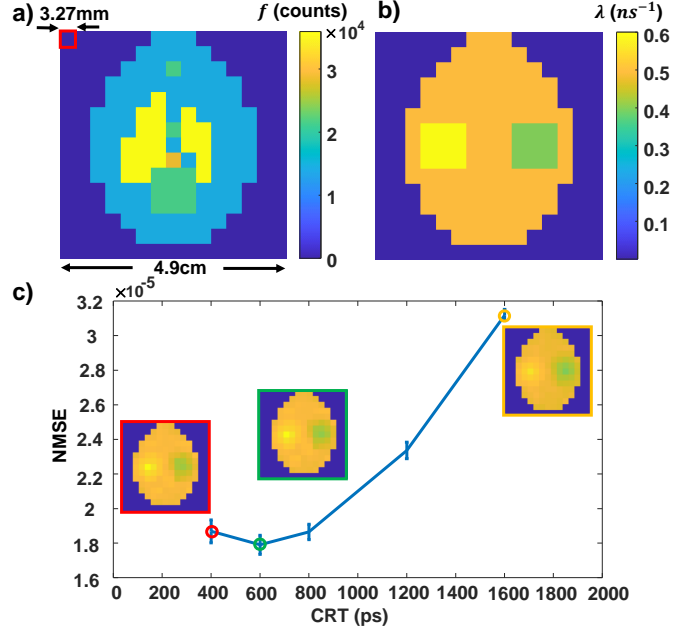


Fig. 5. ML estimation of the decay rate constant map under different CRTs. (a) Activity and (b) decay rate constant map of a 4.9 cm phantom with pixel size of 3.27 mm used for the ML reconstructions under different CRTs. (c) NMSE as a function of CRT. The insets show the reconstructed decay rate constant maps from CRTs 400, 600, and 1600 ps.

found in tomography. When the CRT can cover the entire phantom, such as 600 ps or higher, a larger CRT contributes to higher error in the estimated lifetime $\hat{\tau}_k$ associated with each event, leading to higher error in the reconstructed decay rate constant map.

V. SUMMARY AND DISCUSSIONS

We developed an ML algorithm for reconstructing the positronium lifetime image from LM data acquired by a TOF PET system having that is extended to detect triple coincidences when a $\beta^+ + \gamma$ isotope such as Sc-44 is used. We conducted computer-simulation studies for a 2-d TOF PET system whose configuration parameters are close to existing clinical TOF PET systems (288 detectors on a 57 cm diameter ring and a 570 ps CRT). We considered two numerical phantoms and showed that the proposed reconstruction method was successful. The resulting lifetime images showed good contrast and sharpness and were quantitatively accurate. There were no cross-talks from the activity image.

However, our studies have neglected attenuation, scatter, and random events. Since PLI events are triple-coincidence events, their number can be significantly limited unless a highly sensitive system is used (hence, total-body systems are recommended for PLI [16], [17]). The potential degrading effects of attenuation, scatter, and randoms on the reconstruction of lifetime images need to be investigated. The performance of the reconstruction method for low-count data needs to be studied more thoroughly.

The proposed reconstruction method was based on τ that is not directly measured, and we used its estimate derived from the measured attributes. Given 570 ps CRT, the statistical error

in $\hat{\tau}_k$ obtained by using Eq. (15) can be as large as 0.6 ns. In comparison, the positronium lifetime in our phantoms has a mean of 2 ns. As the statistical error in $\hat{\tau}_k$ is relatively small compared to the value of τ_k itself, ML results agree with the ground truth well. This may not be the case when a 3-d system is considered. To address this issue, in the future study we will investigate formulation of a likelihood function for the estimated $\hat{\tau}_k$ or directly based on the observable attributes.

Currently, consideration for 64×64 images and a relatively large 3.27 mm square pixel is due to the computing resources available and our use of a pre-computed \mathbf{H} . Nonetheless, they are suitable for the purpose of validating the proposed method in principle. Alternative implementation strategies and use of parallel computing will be explored for the development of algorithms suitable for real 3-d TOF PET systems.

ACKNOWLEDGMENT

The contents of this article are solely the responsibility of the authors and do not necessarily represent the official views of the National Institutes of Health or the National Science Foundation. This work was partially supported by NSF grant DMS-1924792 and NIH grant R01-EB029948.

APPENDIX

In PLI, the emitting positrons from pixel j represent a spatiotemporal point process that obeys a Poisson process with rate f_j . Consequently, the number of the positron emissions follows a Poisson distribution with rate $f_j dt$ during the scan within time interval dt . Let $Pr(c_k, \tau_k, j | \boldsymbol{\lambda}, \mathbf{f})$ denote the probability of a detected event to originate in pixel j and take the event (c_k, τ_k) given \mathbf{f} , the voxelized image of the concentration of the PET isotope, and $\boldsymbol{\lambda}$, the voxelized image of the decay rate constant. We assume that all $f_j \geq 0$ and $\lambda_j \geq 0$; i.e., all \mathbf{f} and $\boldsymbol{\lambda}$ images' pixel values are nonnegative. Then the probability of an event (c_k, τ_k, j) given $(\boldsymbol{\lambda}, \mathbf{f})$ is the number of positron emissions with τ_k detected by channel c_k from pixel j (defined as n_1) divided by the number of all possible outcomes (defined as n_2). The discrete approximation of the event probability within with the infinitesimal time interval $d\tau_k$ that might be the bin width used for time discretization is derived as follows:

$$Pr(c_k, \tau_k, j | \boldsymbol{\lambda}, \mathbf{f}) = \frac{n_1}{n_2}, \quad (19)$$

where

$$n_1 \approx (f_j dt) H_{c_k, j} \left(\lambda_j e^{-\lambda_j \tau_k} d\tau_k \right) \quad (20)$$

is the expected number of detected events within time interval dt that originate in pixel j at the k th channel and time delay (c_k, τ_k) given \mathbf{f} and $\boldsymbol{\lambda}$, and

$$\begin{aligned} n_2 &\approx \sum_j \sum_k \int_{\tau_k} (f_j dt) H_{c_k, j} \left(\lambda_j e^{-\lambda_j \tau_k} d\tau_k \right) \\ &= \sum_j \sum_k (f_j dt) H_{c_k, j} \left(\int_{\tau_k} \lambda_j e^{-\lambda_j \tau_k} d\tau_k \right) = \sum_j \sum_k H_{c_k, j} (f_j dt) \end{aligned} \quad (21)$$

is the expected number of detected events within time interval dt over all possible values of (j, k) and τ_k given \mathbf{f} and $\boldsymbol{\lambda}$. Here dt is canceled out in the ratio (19), and $H_{c_k, j} \left(\lambda_j e^{-\lambda_j \tau_k} d\tau_k \right)$ is the probability of events of positron emissions with τ_k detected by channel c_k that originate in pixel j . We define $\sum_j \sum_k H_{c_k, j} f_j := s_{\mathbf{f}}$. Consequently, $Pr(c_k, \tau_k, j | \boldsymbol{\lambda}, \mathbf{f}) \approx s_{\mathbf{f}}^{-1} H_{c_k, j} f_j \lambda_j e^{-\lambda_j \tau_k} d\tau_k$, and then

$$\begin{aligned} Pr(c_k, \tau_k | \boldsymbol{\lambda}, \mathbf{f}) &= \sum_{j=1}^{N_j} Pr(c_k, \tau_k, j | \boldsymbol{\lambda}, \mathbf{f}) \\ &= s_{\mathbf{f}}^{-1} \sum_{j=1}^{N_j} H_{c_k, j} f_j \lambda_j e^{-\lambda_j \tau_k} d\tau_k. \end{aligned}$$

Without loss of generality, we assume that the residual of the approximation is constant with respect to \mathbf{f} and $\boldsymbol{\lambda}$, and then we obtain the probability density function

$$p(c_k, \tau_k | \boldsymbol{\lambda}, \mathbf{f}) = s_{\mathbf{f}}^{-1} \sum_{j=1}^{N_j} H_{c_k, j} f_j \lambda_j e^{-\lambda_j \tau_k}. \quad (22)$$

Assume independent event detection and consider preset-count (PC) acquisition that terminates imaging when exactly N_k events are acquired. Then,

$$p(\mathcal{W}_{N_k}^0 | \boldsymbol{\lambda}, \mathbf{f}) = \prod_{k=1}^{N_k} p(c_k, \tau_k | \boldsymbol{\lambda}, \mathbf{f}), \quad (23)$$

where $\mathcal{W}_{N_k}^0 = \{(c_k, \tau_k)\}_{k=1}^{N_k}$ is the PLI LM data when τ_k is available (e.g. if the system has a perfect TOF resolution). The log-likelihood for the PC-case is therefore given by

$$\ell(\boldsymbol{\lambda}, \mathbf{f}; \mathcal{W}_{N_k}^0) = \sum_{k=1}^{N_k} \log \left(\sum_{j=1}^{N_j} H_{c_k, j} f_j \lambda_j e^{-\lambda_j \tau_k} \right) - N_k \log s_{\mathbf{f}}. \quad (24)$$

For the preset-time (PT) acquisition that conducts imaging for a fixed duration T , N_k is a random number following the Poisson distribution having the mean $\bar{N}_k(T, \mathbf{f}) = T s_{\mathbf{f}}$. Then,

$$p(\mathcal{W}_{N_k}^0 | \boldsymbol{\lambda}, \mathbf{f}, T) = p(\mathcal{W}_{N_k}^0 | \boldsymbol{\lambda}, \mathbf{f}) p(N_k | \bar{N}_k(T, \mathbf{f})), \quad (25)$$

and, within a constant, the PT-case log-likelihood equals

$$\ell(\boldsymbol{\lambda}, \mathbf{f}; \mathcal{W}_{N_k}^0, T) = \sum_{k=1}^{N_k} \log \left(\sum_{j=1}^{N_j} H_{c_k, j} f_j \lambda_j e^{-\lambda_j \tau_k} \right) - T s_{\mathbf{f}}, \quad (26)$$

Observing that the 2nd term on the right-hand side of these log-likelihoods depends only on the total activity of \mathbf{f} through $s_{\mathbf{f}}$, we claim that the maximizing solution of their common term

$$\ell'(\boldsymbol{\lambda}, \mathbf{f}; \mathcal{W}_{N_k}^0) = \sum_{k=1}^{N_k} \log \left(\sum_{j=1}^{N_j} H_{c_k, j} f_j \lambda_j e^{-\lambda_j \tau_k} \right) \quad (27)$$

gives equivalent PC and PT-case ML estimates within a positive scaling factor. To verify, we begin by constructing

$$\ell(\boldsymbol{\lambda}, \xi \mathbf{f}; \mathcal{W}_{N_k}^0, T) = \ell(\boldsymbol{\lambda}, \mathbf{f}; \mathcal{W}_{N_k}^0) + \{N_k \log(\xi s_{\mathbf{f}}) - \xi T s_{\mathbf{f}}\}. \quad (28)$$

This equation indicates that $(\boldsymbol{\lambda}, \xi \mathbf{f})$ maximizes the PT log-likelihood if $(\boldsymbol{\lambda}, \mathbf{f})$ maximizes the PC log-likelihood and ξ maximizes the term in braces in Eq. (28), which can be shown

to be $\xi = N_k/(Ts_f)$. Therefore, the PC-case and PT-case ML estimates are identical up to a positive scale factor (i.e., the normalization constant). Next, we observe that Eq. (24) is invariant to a nonzero scale of \mathbf{f} , so the PC-case ML estimate is unique up to a nonzero scale factor. Hence, when maximizing Eq. (24) we can add a condition $s_f = \zeta$ for any $\zeta > 0$. It can be checked that if $(\mathbf{f}, \boldsymbol{\lambda})$ maximizes Eq. (24) subject to $s_f = \zeta_1$, then $((\zeta_2/\zeta_1)\mathbf{f}, \boldsymbol{\lambda})$ maximizes Eq. (26) subject to $s_f = \zeta_2$. This shows that PC-case solutions under various $s_f = \zeta$ constraints are identical up to a scale factor. Now, maximizing Eq. (24) subject to $s_f = \zeta$ is the same as maximizing Eq. (27). Since ζ can be any positive number, it follows that we can simply seek maximization of Eq. (27).

By integrating Eq. (23) over each τ_k , taking logarithm and applying similar arguments, we show that, within a nonzero scaling factor, the ML \mathbf{f} of the TOF PET LM data \mathcal{C}_N can be obtained by maximizing

$$\ell'(\mathbf{f}; \mathcal{C}_N) = \sum_{k=1}^{N_k} \log \left(\sum_{j=1}^{N_j} H_{c_k,j} f_j \right). \quad (29)$$

REFERENCES

- [1] P. Moskal, D. Kisielewska, C. Curceanu, E. Czerwiński, K. Dulski, A. Gajos, M. Gorgol, B. Hiesmayr, B. Jasińska, K. Kacprzak *et al.*, “Feasibility study of the positronium imaging with the J-PET tomograph,” *Physics in Medicine & Biology*, vol. 64, no. 5, p. 055017, 2019.
- [2] P. Moskal, B. Jasińska, E. Stepien, and S. D. Bass, “Positronium in medicine and biology,” *Nature Reviews Physics*, vol. 1, no. 9, pp. 527–529, 2019.
- [3] K. Ote and F. Hashimoto, “Deep-learning-based fast TOF-PET image reconstruction using direction information,” *Radiological Physics and Technology*, vol. 15, no. 1, pp. 72–82, 2022.
- [4] M. D. Harpen, “Positronium: Review of symmetry, conserved quantities and decay for the radiological physicist,” *Medical Physics*, vol. 31, no. 1, pp. 57–61, 2004.
- [5] K. Shibuya, H. Saito, F. Nishikido, M. Takahashi, and T. Yamaya, “Oxygen sensing ability of positronium atom for tumor hypoxia imaging,” *Communications Physics*, vol. 3, no. 1, p. 173, 2020.
- [6] P. Moskal and E. Stepien, “Positronium as a biomarker of hypoxia,” *Bio-Algorithms and Med-Systems*, vol. 17, no. 4, pp. 311–319, 2021.
- [7] P. Moskal, K. Dulski, N. Chug, C. Curceanu, E. Czerwiński, M. Dadgar, J. Gajewski, A. Gajos, G. Grudzień, B. C. Hiesmayr *et al.*, “Positronium imaging with the novel multiphoton pet scanner,” *Science advances*, vol. 7, no. 42, p. eabh4394, 2021.
- [8] P. Moskal, A. Gajos, M. Mohammed, J. Chhokar, N. Chug, C. Curceanu, E. Czerwiński, M. Dadgar, K. Dulski, M. Gorgol *et al.*, “Testing cpt symmetry in ortho-positronium decays with positronium annihilation tomography,” *Nature communications*, vol. 12, no. 1, p. 5658, 2021.
- [9] J. S. Karp, V. Viswanath, M. J. Geagan, G. Muehllehner, A. R. Pantel, M. J. Parma, A. E. Perkins, J. P. Schmall, M. E. Werner, and M. E. Daube-Witherspoon, “Pennpet explorer: design and preliminary performance of a whole-body imager,” *Journal of Nuclear Medicine*, vol. 61, no. 1, pp. 136–143, 2020.
- [10] B. A. Spencer, E. Berg, J. P. Schmall, N. Omidvari, E. K. Leung, Y. G. Abdelhafez, S. Tang, Z. Deng, Y. Dong, Y. Lv *et al.*, “Performance evaluation of the uexplorer total-body pet/ct scanner based on nema nu 2-2018 with additional tests to characterize pet scanners with a long axial field of view,” *Journal of Nuclear Medicine*, vol. 62, no. 6, pp. 861–870, 2021.
- [11] I. Alberts, J.-N. Hünermund, G. Prenosil, C. Mingels, K. P. Bohn, M. Viscione, H. Sari, B. Vollnberg, K. Shi, A. Afshar-Oromieh *et al.*, “Clinical performance of long axial field of view pet/ct: a head-to-head intra-individual comparison of the biograph vision quadra with the biograph vision pet/ct,” *European journal of nuclear medicine and molecular imaging*, vol. 48, pp. 2395–2404, 2021.
- [12] J. Qi and B. Huang, “Positronium lifetime image reconstruction for tof pet,” *IEEE Transactions on Medical Imaging*, 2022.
- [13] T. Matulewicz, “Radioactive nuclei for β^+ γ pet and theranostics: selected candidates,” *Bio-Algorithms and Med-Systems*, vol. 17, no. 4, pp. 235–239, 2021.
- [14] J. Choiński and M. Łyczko, “Prospects for the production of radioisotopes and radiobioconjugates for theranostics,” *Bio-Algorithms and Med-Systems*, vol. 17, no. 4, pp. 241–257, 2021.
- [15] R. L. Siddon, “Fast calculation of the exact radiological path for a three-dimensional ct array,” *Medical physics*, vol. 12, no. 2, pp. 252–255, 1985.
- [16] P. Moskal, D. Kisielewska, R. Y. Shopa, Z. Bura, J. Chhokar, C. Curceanu, E. Czerwiński, M. Dadgar, K. Dulski, J. Gajewski *et al.*, “Performance assessment of the 2 γ positronium imaging with the total-body PET scanners,” *EJNMMI physics*, vol. 7, no. 1, pp. 1–16, 2020.
- [17] P. Moskal and E. Stepien, “Prospects and clinical perspectives of total-body PET imaging using plastic scintillators,” *PET clinics*, vol. 15, no. 4, pp. 439–452, 2020.